GTP-18-1453

VOLUMETRIC VELOCIMETRY MEASUREMENTS OF FILM COOLING JETS

Artur Joao Carvalho Figueiredo ajcbsd20@bath.ac.uk
Robin Jones R.R.Jones@bath.ac.uk
Oliver J. Pountney O.J.Pountney@bath.ac.uk
James A. Scobie J.A.Scobie@bath.ac.uk
Gary D. Lock G.D.Lock@bath.ac.uk
Carl M. Sangan C.M.Sangan@bath.ac.uk
David J. Cleaver D.J.Cleaver@bath.ac.uk

Department of Mechanical Engineering
University of Bath
Bath, BA2 7AY
United Kingdom

ABSTRACT

This paper presents Volumetric Velocimetry (VV) measurements for a jet in crossflow that is representative of film cooling. Volumetric velocimetry employs particle tracking to non-intrusively extract all three components of velocity in a three-dimensional volume. This is its first use in a film-cooling context. The primary research objective was to develop this novel measurement technique for turbomachinery applications, whilst collecting a high-quality data set that can improve the understanding of the flow structure of the cooling jet. A new facility was designed and manufactured for this study with emphasis on optical access and controlled boundary conditions. For a range of momentum flux ratios from 0.65 to 6.5 the measurements clearly show the penetration of the cooling jet into the freestream, the formation of kidney-shaped vortices and entrainment of main flow into the jet. The results are compared to published studies using different experimental techniques, with good agreement. Further quantitative analysis of the location of the kidney vortices demonstrates their lift off from the wall and increasing lateral separation with increasing momentum flux ratio. The lateral divergence correlates very well with the self-induced velocity created by the wall-vortex interaction. Circulation measurements quantify the initial roll up and decay of the kidney vortices and show that the point of maximum circulation moves downstream with increasing momentum flux ratio. The potential for non-intrusive volumetric velocimetry measurements in turbomachinery flow has been clearly demonstrated.

1 INTRODUCTION

The requirement for improved efficiency and power output from gas turbines has led to a steady rise in turbine entry temperature. A direct consequence is the need for coolant flow to protect highly-stressed engine components against overheating and to extend the operational life of the turbine. One method of protecting vanes and blades from thermal stresses is to create a protective layer of coolant between the hot mainstream and the surface of the metal. This is commonly known as film cooling. Superfluous use or poor implementation of the compressed coolant can reduce thermodynamic efficiency. Therefore, this secondary-air-system is of particular interest to the engine designer.

Typically film cooling is introduced through cylindrical or shaped holes and the interaction of the cooling plume and the mainstream flow produces three-dimensional flow structures as shown in Figure 1. Fric and Roshko [1] and Andreopoulos and Rodi [2], among others, describe the main

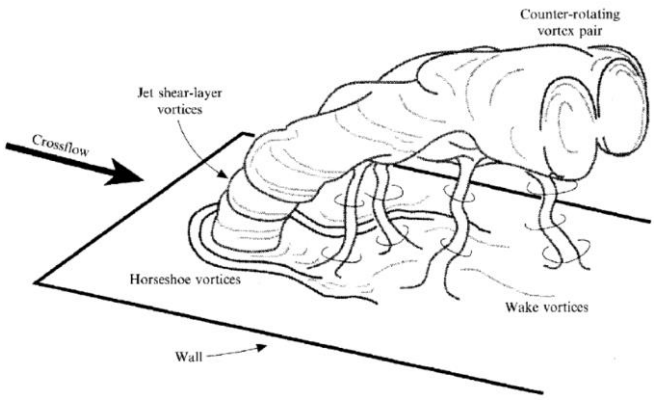

Figure 1: Film cooling flow structures ([1])

Table 1: Comparison of papers on film cooling using optical techniques

Study	*Exp. Tech*	*g/D*	*l/D*	α [deg]	*M*	Re_D	*DR*	*IR*
[6]	LDA	3, 5	≈1	35	0.015	4000	1, 1.5, 2	0.25 → 4.2
[8]	LDA	3	2.8	35, 55	0.03-0.09	7000-22000	1.6	0.08 → 0.63
[13]	S-PIV	4	2.8	30, 50	0.3	32000	1, 1.6	0.65 → 7.2
[14]	LDA/PIV	3, 6.7	4.7	30, 35	<0.05	<11000	1.2, 1.6	0.16 → 3.3
[16]	S-PIV	4	4.66	35	0.03	3000	1	0.25 → 2.25

flow features of film cooling: a jet that penetrates into the freestream, a counter-rotating vortex pair (or kidney vortex), jet shear-layer vortices, wake vortices and a system of horseshoe vortices.

At low injection rates, the coolant remains close to the wall, creating a protective layer of low-temperature flow between the vulnerable metal wall and the high-temperature mainstream. For high injection rates, the jet penetrates into the mainstream with a curved trajectory. A pair of counter-rotating vortices is created by the impulse of the jet on the crossflow; the cross-section of the jet is modified to a kidney-shaped form which dominates the structure in the far field. These so-called *kidney vortices* are an important part in the mixing of main and coolant flows, thus affecting the performance of film cooling. The main focus of this paper is to explore these structures using volumetric velocimetry.

There is a vast experimental and computational literature related to film cooling: [3] and [4] provide general reviews. Transient facilities are commonly used when assessing heat-transfer performance, while steady-flow rigs provide a more appropriate test bench for studying the parameters that influence the governing fluid-dynamics. While some facilities operate in cascades or engine-representative geometries, the majority investigate film cooling on a flat plate.

The flow structure of coolant jets has been studied extensively. Examples include Wilfert and Fottner [5], who found that the position of the horse-shoe vortex was strongly dependent on the blowing ratio, with a relevant influence in the mixing mechanisms. Peña and Arts [6] studied the flow-field generated by a row of inclined cooling holes and the interaction between the jets, and concluded that the momentum flux ratio characterized the interaction between the jet and the incoming boundary layer. Goldstein *et al.* [7] assessed the effects of geometry and density when injecting cooling flow through a row of discrete holes. Both blowing ratio (*e.g.* Wilfert and Fottner [5]) and momentum flux ratio (*e.g.* [8]) are employed for characterizing findings in film cooling studies. The definitions for these parameters are available in the nomenclature.

There is a growing trend and requirement to use numerical simulation to predict cooling performance. CFD can provide insight into the physics of film cooling (*e.g.* [9-11]) but accurate modelling of the flow structure depends strongly on the calculation of mixing between the jet and crossflow; this is limited by turbulence models and computations require experimental validation.

Experimental exploration of the three-dimensional (3D) flow structures in the jet requires a non-intrusive measurement technique. Optical methods have been employed to conduct velocity measurements in turbomachinery rigs, despite the difficulty of access for both laser and camera in a typically closed and confined environment. Woisetschläger and Göttlich [12] provide a review of Particle Image Velocimetry in engine-simulated environments.

Of particular interest to this paper are film cooling experiments using cylindrical holes on flat plates where optical techniques have been employed. The data in these papers is particularly useful to fulfil the objective of applying and developing a novel optical technique. An overview of five relevant studies is provided in Table 1. The two main techniques used are Laser Doppler Anemometry (LDA) and Particle Image Velocimetry (PIV). Two examples of LDA are Peña and Arts [6] and Kohli and Bogard [8]. The first studied the flow structure of both a single jet and a row of jets for different pitch-to-diameter ratios (*g/D*), density ratios (*DR*) and momentum flux ratios (*IR*) and mainstream Mach numbers (*M*). These variables are defined in the nomenclature. The latter study [8] assessed the effectiveness of a row of holes with a large injection angle.

More recent studies have employed PIV or even Stereo-PIV (S-PIV), capable of producing two-dimensional-two-component (2D-2C) and 2D-3C velocity fields, respectively. Bernsdorf *et al.* [13] used S-PIV with different injection angles (α), density ratios (*DR*) and momentum flux ratios (*IR*). Eberly and Thole [14] used LDA and PIV to study the flow-field of film cooling jets with a range of density and momentum flux ratios, along with two different geometries.

Beyond cylindrical holes, Laveau and Abhari [15] used S-PIV to study the flow structure of film cooling emerging from shaped holes. S-PIV was also employed by Wright *et al.* [16] in a study that compared three different geometries: traditional cylindrical holes, fan shaped holes and a double hole geometry comprising of two compound angle holes. Schroeder and Thole [17] tested the influence of high freestream turbulence on the flow-field of shaped holes, finding little effect on the mean velocities of the jet but increased lateral spreading of the coolant due to increased turbulence intensity around the jet.

Objectives

To fully understand the three-dimensional flow structures associated with film cooling requires a non-intrusive measurement technique that captures all three components of velocity inside a three-dimensional volume. Bernsdorf *et al.* [13] measured the full three-dimensional flow-field through the superposition of multiple, time-averaged slices of 2D-3C data taken at different times. In this paper the application of a new volumetric velocimetry technique, TSI-V3V (Volumetric 3-component Velocimetry), is developed; this method directly enables 3D-3C measurements. V3V in air has never been applied to a turbomachinery rig and its first use in a film-cooling context is demonstrated. There are few

publications related to V3V, with most conducted using water as a medium (*e.g.* [18, 19]) and very few conducted in a gas medium (*e.g.* [20]). Extracting the velocity field provides an invaluable, high-quality data set appropriate to validate computational fluid dynamics, and improve the fundamental understanding of the fluid dynamics governing film cooling.

To enable volumetric velocimetry measurements of film cooling a new continuous open-loop experimental facility was designed specifically for optical access. The rig features a flexible, modular test section that enables pressure, hot-wire and volumetric velocimetry measurements. An upstream suction-bleed mechanism allows control of the boundary layer. All tests were carried out at a low turbulence level.

The rig was designed to simulate the experimental conditions of Bernsdorf *et al.* [13], *e.g., g/D, l/D, α, DR* and *M*. This study was selected from a list available in Table 1 because S-PIV is the closest optical measurement technique to volumetric velocimetry. The current rig is capable of a wide range of momentum-flux ratios using CO_2 as coolant flow with a $DR = 1.52$.

The TSI-V3V system for volumetric velocimetry measurements is introduced in Section 2. The design and commissioning of the new facility is described in Section 3. The VV data for film cooling jets emerging over a range of momentum flux ratio is presented in Section 4, including a comparison with [13].

2 VOLUMETRIC VELOCIMETRY

The volumetric velocimetry (VV) system used here is known as V3V, the trademark name associated with TSI; this is an experimental technique for measuring three-component velocity in 3D space. VV can be understood as a 3D version of traditional PIV, which is a well-established experimental technique in fluid dynamics. However, there are several significant differences between traditional PIV and VV: PIV generally uses one or two cameras with image correlation of discretized windows (each window includes multiple particles) to extract a 2D-2C or 2D-3C velocity field; VV uses a direct particle-tracking approach in three-dimensional space to extract a 3D-3C flow-field (this requires three cameras).

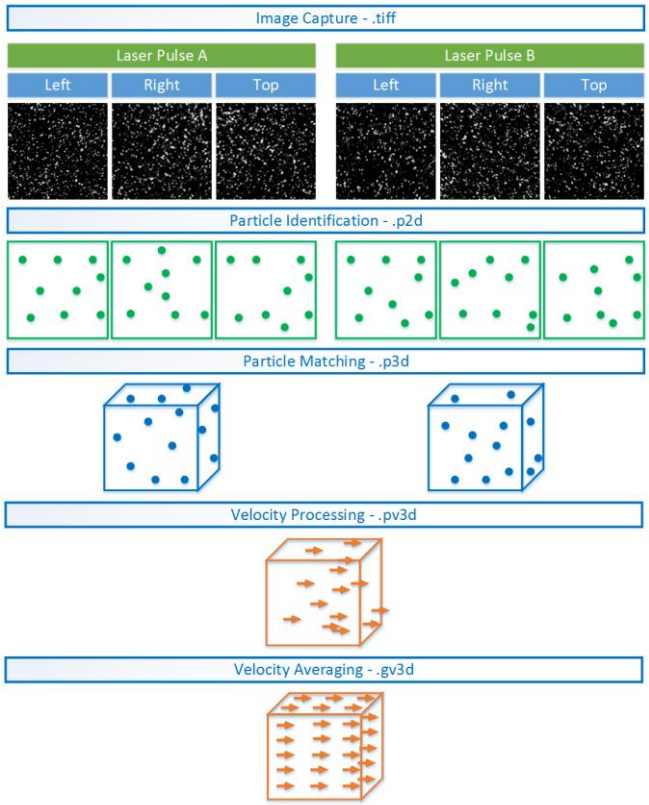

Figure 2: Basic Steps of VV

VV and PIV require different methods and approaches, and consequently the equipment, calibration and processing of these systems are also different. The VV method for determining the velocity field is composed of five phases, as depicted schematically in Figure 2. The Image-Capture Phase consists of taking three simultaneous frames of the flow (one with each camera) at each laser pulse, resulting in six tiff files per capture. The interrogated region is illuminated by a laser *cone*, not a laser *sheet* as used in PIV. The entire measurement volume is consequently captured at each instant and no volume reconstruction is required in post processing.

The image processing starts with the Particle-Identification Phase. The software runs through all the frames and identifies individual particles, with the intensity of each particle fitted to a 2D Gaussian. A file containing the particle positions per frame is created. In the Particle-Matching Phase the software determines the 3D coordinates of each particle by applying a calibration polynomial to the particles in the three frames captured at each laser pulse. A particle with a known position in 3D space is known as a triplet. A file with a 3D particle geometry cloud is generated per laser pulse and per capture. In the Velocity-Processing Phase the algorithm tracks each triplet individually, identifying the same triplet in the next laser pulse. Different tracking algorithms are available; here Robust Point Matching was recommended by TSI as it is especially suited for highly-seeded flows. Details on the algorithm can be found in Stellmacher and Obermayer [21]. At the end of this Phase, one file is generated per capture, containing the 3D coordinates of the particles and the associated components of the velocity vectors determined during the processing. Finally, the last phase (Velocity Averaging) generates a structured grid of a pre-determined spatial resolution and applies a Gaussian-weighted average of the instantaneous vectors within each voxel to produce one average velocity vector, effectively time-averaging similar to 2D and S-PIV. The Gaussian weighting is related to the position of the instantaneous vectors within the voxel. Vectors closer to the centre of the voxel have a larger weight than those at the edge. No interpolation is performed and all vectors are a direct result of the averaging of the instantaneous vectors measured by the VV system.

Droplet generators (described below in Section 3) were employed to generate seeding tracers. The ability of a particle to follow the flow is determined by the Stokes number (*St*): the ratio between the characteristic response time of a particle to the characteristic flow time-scale. Using the definition for the Stokes number, the value $St = 0.024 \pm 0.025$ was calculated for these experiments. The characteristic length scale chosen was the minimum bend radius experienced by a particle in the coolant flow as its trajectory is bent after exiting the film cooling hole. The bend radius was computed using the information available in the literature (Bernsdorf [22]) on the jet's centreline path. A velocity of 150 m/s was used for calculating the Stokes number, the maximum

instantaneous velocity expected at any point in the measurement volume during this experimental campaign. According to Tropea *et al.* [23], St<0.1 delivers "an acceptable flow tracing accuracy with errors below 1%". The low Stokes number validates the use of particle tracking measurement techniques for the experiments conducted here.

The particles were illuminated using a Quantel EverGreen 200 mJ laser at 532 nm with plano-cylindrical concave lenses to generate a laser cone. These devices are connected to a LaserPulse Synchronizer Model 610036 with a temporal resolution of 0.25 ns. A dedicated computer runs the acquisition system using TSI Insight V3V software.

The illuminated particles were captured through three 8MP CCD cameras, each with resolution 3312 x 2488 pixels coupled with 75 mm lenses. These cameras were spatially calibrated by traversing a plate at 0.25 mm intervals with a known dot pattern through the *z*-axis of the camera assembly. The 2D images were then used to create a polynomial-function relating particle position in the frame to real position in 3D space. The captures were taken through the glass window that provides optical access to the test section in the film cooling rig.

In terms of image capturing, seven different cases were tested, with 500 captures taken per case. The two laser pulses were separated by 3.5 μs. The usual procedure for choosing the time-step in laser techniques is to adjust it to the dominant velocity component of the flow; this ensures the maximum particle displacement between the two frames is between 5 to 10 pixels. It was found that such a criterion could not be applied in this situation. Here the dominant velocity is the *u*-component (freestream, U_∞), though the components of greatest interest are the *v* and *w* (associated with the kidney vortices) which have much smaller velocities (< 0.1U). Optimising the laser pulse time-step (Δt) for the *u*-component would consequently generate excessive noise in the *v*- and *w*-components (due to the small particle displacements). A longer laser pulse Δt of 3.5 μs was thus chosen. The only drawback of choosing a longer laser pulse Δt is that any small scale flow features in the *u*-component will be lost, not a concern, and the software may find it harder to pair the particles between frame A and B, as the particle displacement in *u* is very large. As a consequence, the number of vectors found will be smaller, demanding more captures to achieve higher quality results and a better spatial resolution. All processing used the TSI Insight V3V software. For each case of 500 captures the processing time was approximately 12 hours on a PC with a 24-core CPU and 128 Gb RAM. No global and local validation filters were used during the processing, which delivered results in as raw a form as possible. No overlap or smoothing were used for plotting the results. The spatial resolution was a voxel of 1 mm x 1 mm x 1 mm. On average, each voxel contained about 450 instantaneous velocity vectors that were averaged to find the final results plotted here. The position of the wall was computed using the volumetric velocimetry system itself: the tunnel with no flow was captured and wall reflections were used to define the *z*-coordinate, and the reflections from the edges of the film cooling holes used to define the *x*- and *y*-coordinates. The full measured volume has dimensions of approximately 65 mm x 45 mm x 10 mm. Post-processing was carried out in Matlab R2014b, including the calculation of vorticity (see nomenclature) with derivatives computed using central finite differences with fourth-order accuracy. Only the region of interest was investigated, with dimensions of approximately 52 mm x 16 mm x 8 mm. This corresponds to a volume that starts 4D upstream of the reference frame and ends 9D downstream. The y coordinate varies between y = ±2D and the z coordinate ranges from z = 0 at the wall to z = 2D.

2.1 Uncertainty analysis

Uncertainty analysis was performed using the standard procedures outlined by Moffat [24-26]. The magnitude of the velocity is given by $|\vec{V}| = |\Delta\vec{r}|/\Delta t$, where $|\Delta\vec{r}| = \sqrt{\Delta x^2 + \Delta y^2 + \Delta z^2}$. Therefore, the uncertainty in velocity magnitude is given by:

$$\varsigma|\vec{V}| = \pm\sqrt{\left(\frac{\Delta x}{|\Delta\vec{r}|\Delta t}\varsigma(\Delta x)\right)^2 + \left(\frac{\Delta y}{|\Delta\vec{r}|\Delta t}\varsigma(\Delta y)\right)^2 + \left(\frac{\Delta z}{|\Delta\vec{r}|\Delta t}\varsigma(\Delta z)\right)^2 + \left(\frac{|\Delta\vec{r}|}{\Delta t^2}\varsigma(\Delta t)\right)^2}$$

If we consider the direction of the vector in spherical coordinates with $\zeta = \tan^{-1}(y/x)$ and $\varphi = \cos^{-1}(z/|\vec{r}|)$, the uncertainty is given by:

$$\varsigma\zeta = \pm\sqrt{\left(\frac{\cos^2\zeta}{\Delta x}\varsigma(\Delta x)\right)^2 + \left(\frac{\Delta y\cos^2\zeta}{\Delta x^2}\varsigma(\Delta y)\right)^2}$$

$$\varsigma\varphi = \pm\sqrt{\left(\frac{\Delta z\Delta x}{|\Delta\vec{r}|^3\sin\varphi}\varsigma(\Delta x)\right)^2 + \left(\frac{\Delta z\Delta y}{|\Delta\vec{r}|^3\sin\varphi}\varsigma(\Delta y)\right)^2 + \left(\frac{\Delta x^2+\Delta y^2}{|\Delta\vec{r}|^3\sin\varphi}\varsigma(\Delta z)\right)^2}$$

The software resolves the position of the particle in each image using a Gaussian fit. The 2D Gaussian peak position uncertainty is $\sim \pm 0.1$ pixels. The least squares error (mean *dewarping* error) of the calibration contributed a position uncertainty of $\pm$ 0.5 pixels. The displacement vector components are computed from six images of any given particle. The uncertainty in Δx and Δy is dominated by the average displacement of the triplet and was estimated to be ± 0.5 pixels. The uncertainty in Δz is scaled by the triangulation of the triplet and was estimated to be $\pm$ 2 pixels (1 pixel ≈ 20 μm). The time step between laser pulses was $\Delta t = 3.5$ μs with an uncertainty of $\pm$ 7 ns which is limited by the half-width-half-maximum of the pulses. The average of the u, v and w magnitudes was typically 100, 1.8 and 2.5 m/s respectively and is used to compute reference values of Δx, Δy and Δz. Using the formulae above, the uncertainty in $|\vec{V}|$ for a single capture was estimated to be $\pm$ 3 %. The uncertainty in ζ and φ was computed to be $\pm$ 2° and $\pm$ 6° respectively. With the exception of $\varsigma\varphi$, the most significant contribution came from the terms involving Δx which were an order of magnitude larger than those involving Δt and two orders larger than those involving Δy and Δz. $\varsigma\varphi$ was most significantly contributed to by the propagation of Δz.

For a generic time-averaged VV data set consisting of $n =$ 500 instantaneous vector fields, the vector standard deviation

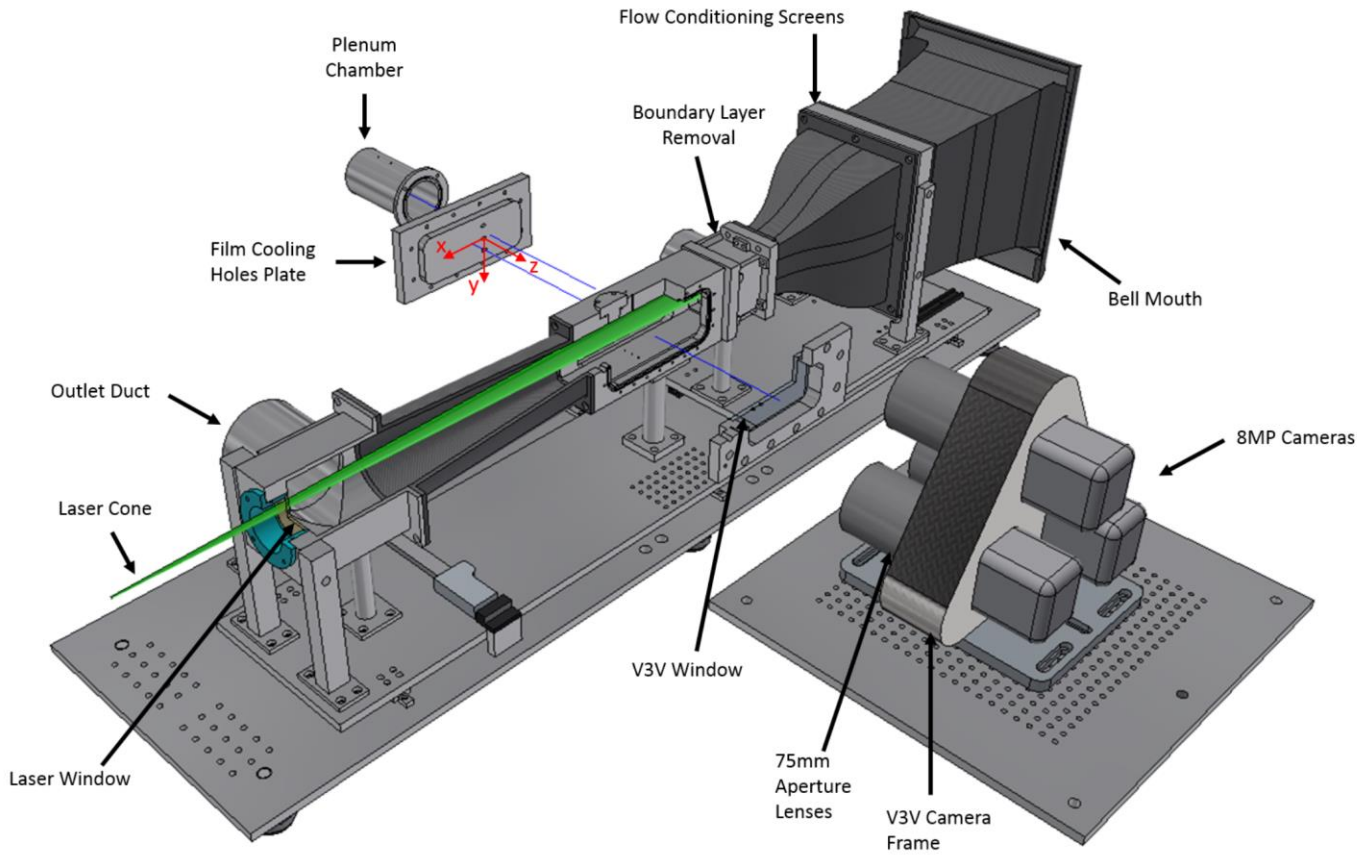

Figure 3: Illustration of the film cooling rig

($\sigma|\vec{V}|$) was typically less than 15 m/s. Hence, the upper limit of the statistical error on the mean velocity vectors is $\varsigma|\vec{V}| = \sigma|\vec{V}|/\sqrt{n} = 0.7$ m/s (approximately 0.7% of the freestream velocity).

3 EXPERIMENTAL FACILITY

The main design aim of the new test rig was to study film cooling using volumetric velocimetry. The design also supports pressure, concentration, hot-wire, temperature and PLIF (Planar Laser-Induced Fluorescence) measurements. A schematic view of the main components of the facility is shown in Figure 3, including the main body of the wind tunnel, the bedplate and fittings that support the tunnel. The three camera assembly is shown in Figure 3 positioned in front of the test section. Two plates are also displayed in an exploded view of the test section. The modular design of the rig allows easy switching between plates for different measurements.

A vacuum pump attached to the outlet duct draws air from the laboratory into the rig through a bell-mouthed inlet. The bell-mouth was designed according to Ito *et al.* [27] so as to ensure uniform inlet flow. The air passes through two downstream screens: a honeycomb to straighten the flow and a turbulence screen to ensure low turbulence flow. A contraction nozzle provides a smooth transition to the core of the wind tunnel which includes boundary-layer removal and the main test section. The screens and contraction nozzle were designed using well-established guidelines [28, 29]. Variable-controlled suction is used to control the thickness of the boundary layer in the test section.

The test section features a constant rectangular cross-section of 54x40 mm^2, with three film cooling holes on the back 54 mm face. These holes are supplied from a plenum chamber and a pressurised, metered line of CO_2. The flow is diffused immediately downstream of the test section; it is subsequently turned 90° before exiting the facility to the vacuum pump. The region of interest was illuminated from the end of the tunnel using the laser window labelled in Figure 3. The beam is diverged into a cone, as shown in Figure 3, with the help of plano-cylindrical lenses.

The operating point of the rig was designed to simulate the experimental conditions of Bernsdorf *et al.* [13], as shown in Table 2. There are some differences between the rigs, *e.g.*, the diameter of the cooling holes and boundary layer

Table 2: Direct comparison with [13]

Parameter	[13]	Bath
M	0.3	0.3
D [mm]	5	4
g/D	4	4
l/D	2.8	2.8
α [deg]	30	30
δ*/D	0.117	0.12
θ/D	0.051	0.09
H	2.3	1.29
# of holes	7	3

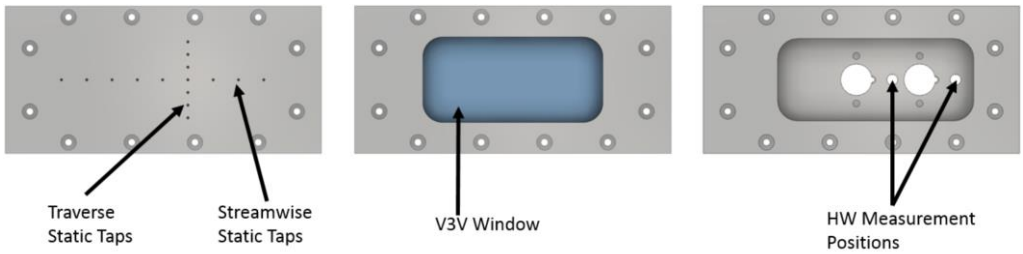

Figure 4: Different plates used in the film cooling rig: a) Static Taps (left), b) VV (centre) and c) Hot-Wire (right)

characteristics. The capacity of the Bath rig is shown in Table 3, alongside the typical pressure-side cooling ranges expected in an engine [13]. The Bath rig is capable of a wide range of momentum-flux ratios ($0.1 < IR < 7$) at the operating point, using 100% CO_2 as coolant flow with a $DR = 1.52$.

Table 3: Capacity of the new test rig

Parameter	Typical pressure-side film cooling range [13]	Bath rig
M	0.3→0.8	0.1→0.34
DR	1→1.8	1→1.52
IR	0.9→2	0.1→7

Three different, modular aluminium plates were employed on the near face of the test section. The first, shown in Figure 4a, was used to measure the variation of static pressure in the stream-wise and crosswise directions using an array of taps of 0.5 mm in diameter. A second plate, shown in Figure 4c, allowed hot-wire measurements to be taken just upstream of the film cooling hole using a TSI model 1218-20, purposefully designed for boundary-layer measurements. The wire was connected to a constant-temperature anemometer (model TSI 1750) and calibrated *in-situ* with simultaneously-collected data from a pitot-static tube (model Kimo DBM 610 type L) in the same equivalent location in the test section over a range of flow velocities. All pressures were read using an ESI-PR3202 differential transducer with a range of 0-100 mbar and an accuracy of ±0.3% of the full-scale (FS), connected to a ScaniValve scanner with 48 ports.

The third plate, shown in Figure 4b, featured a glass window to allow optical access for the cameras. The glass surface was treated with an oleophobic coating which prevented oil particles from depositing on the surface.

All tests were conducted using the film-cooling geometry shown in Figure 5, with dimensions provided in Table 2. The reference frame used is shown on Figure 5 and in the wind

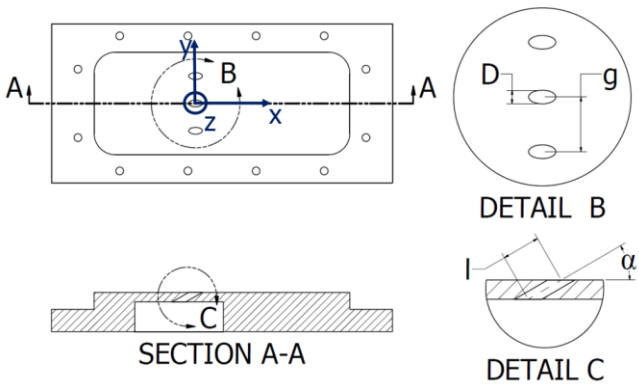

Figure 5: Film Cooling Holes Geometry

tunnel context in Figure 3. The origin of the reference frame is located on the centreline of the cylindrical hole as it meets the surface of the plate. The plate with the cooling holes was mounted into the far-side of the test section. The surface was spray-painted black to provide a suitable, noise-limiting background for the volumetric velocimetry measurements. The surface roughness was assessed in a Proscan 2000 using a chromatic sensor S5/03 with a 300 µm range, a shutter frequency of 1 kHz and a resolution of 0.01 µm. The test comprised 500 steps of 1 µm in both *x* and *y* directions. The computed mean *Ra* was 0.7µm in both directions.

The main flow was driven by a positive-displacement blower (model WADE SRO44-3013). The motor speed was controlled to create a constant Mach number at the test section. The coolant flow was supplied by an array of CO_2 cylinders capable of supplying up to 100 kg/h. The mass flow was regulated using a mass flow controller (model Alicat MCR-1500) calibrated for CO_2 with an accuracy of ±0.08% of reading, ±0.02% of the FS and a range of 0.9 to 180 kg/h. The mass flow was used to compute the momentum flux ratio.

All the measurements were acquired using a National Instruments NI-cDAQ-9174 data acquisition system, controlled through a dedicated computer using an in-house LabView code.

Two droplet generators (TSI 9307-6, with six Laskin nozzles) were used for the VV measurements. These were produced by TSI but modified in-house for the current application. The main-flow droplet generator was driven by a 6-bar workshop air supply. A pressure regulator in the line allowed precise control of the seeding density in the main flow. The seeding was introduced at the bell-mouth inlet using a 2D array of discrete injection points. The coolant-flow droplet generator was placed in parallel with the main coolant flow line. A set of valves allowed precise control of the seeding density of the coolant flow by regulating the percentage of CO_2 that bypassed the seeding generator. DEHS and olive oil were both tested successfully in the experiments as seeding tracers. Beyond surface contamination due to the oil, no noticeable difference in performance was observed.

Commissioning

Two main commissioning tests were conducted to ensure the main flow conditions were set correctly.

The first commissioning experiment used the static taps and pitot probe to measure the variation of velocity at the test section. Figure 6 shows the transverse velocity distribution across the cross-section is constant and without skew. The velocity in the stream-wise direction is shown to increase monotonically along the tunnel. This is evidence that the flow is not fully developed and the growth of the boundary layers

on the wall is effectively constricting the area of freestream along the tunnel.

The second commissioning experiment determined the boundary-layer profile in a position just upstream of the central film cooling hole. This was measured from the hot-wire traversing the flow from the middle of the tunnel to a point 0.23 mm from the wall. The hot-wire features a security pin which ends 0.13 mm below the fragile sensor, avoiding any contact with the wall. This pin was used to find the zero position relative to the wall. Figure 6 shows the velocity profile accurately followed the 1/7th power law for turbulent boundary layers with a boundary layer thickness δ = 3.88 mm. The 1/7th power law was used to calculate the displacement and momentum thicknesses relative to the hole-diameter D, and shape factor: δ^*/D = 0.12, θ/D = 0.09, and H = 1.29.

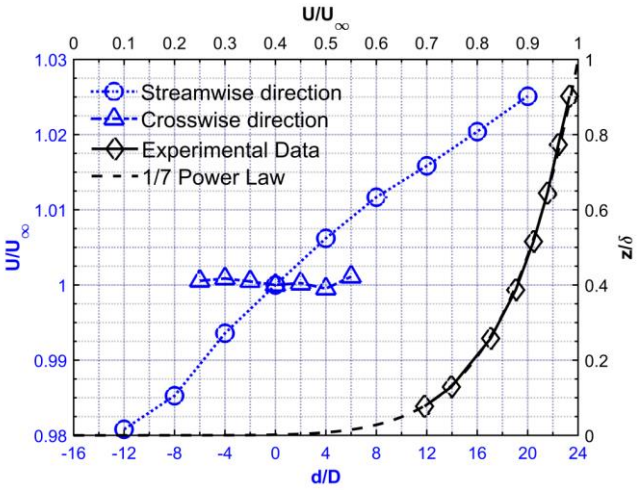

Figure 6: Commissioning results

4 RESULTS

This section illustrates the potential for applying volumetric velocimetry to turbomachinery flows through measurements for film cooling jets in cross-flow. Different plotting schemes (*e.g.* planes, isosurfaces and streamlines) are employed to demonstrate the capability of this technique to capture the highly three-dimensional flowfield. In section 4.1, new data collected in the Bath rig using volumetric velocimetry is compared with results collected by Bernsdorf *et al.* [13] using S-PIV under similar geometric and fluid-dynamic conditions. In Section 4.2, volumetric velocimetry measurements are presented for seven momentum-flux ratios ($0.65 < IR < 6.5$) using 100% CO_2 as coolant flow. In Section 4.3 further analysis of the vortex pair is carried out, including the calculation of the vortex core trajectory and circulation for different IR.

The range of *IR* tested contains two cases typical of design conditions film cooling (*IR* = 0.65 and 1.6). The remaining cases present values of IR higher than typically employed in turbines at design conditions. These higher *IR* cases are chosen to enhance the secondary flow features and hence enable a better assessment of the capabilities of VV. Moreover, they are of special interest to study the behaviour of film cooling for off-design conditions.

Bogard and Thole [3] describe how coolant jets can separate from the surface as they emerge the hole exit and reattach farther downstream. They identified three distinct regimes governed by IR and quantified these for holes orientated in the mainstream direction with an inclination of 35^o relative to the surface. The coolant jets were found to remain attached to the surface for IR < 0.4 and were fully detached for IR > 0.8. For 0.4 < IR < 0.8 the jets were initially detached but reattached a short distance downstream. In this paper the hole angles are 30^o and fully detached jets are expected for all cases other than IR = 0.65. At high IR a pair of counter-rotating vortices is created by the impulse of the jet on the crossflow; the cross-section of the jet is modified to a kidney-shaped form which dominates the structure in the far field.

4.1 Comparison of Volumetric Velocimetry and S-PIV

Figure 7 directly compares volumetric velocimetry results with Stereo PIV measurements from Bernsdorf *et al.* [13] at three common momentum flux ratios *IR* (see nomenclature); the data is shown in the plane at x/D = 4. The stream-wise velocity component u is shown in the contour and the components v and w are displayed as in-plane vectors; all components are non-dimensionalised by the undisturbed free-stream velocity (U_∞). In this figure, comparable contour levels are used for both studies.

Both sets of data show similar qualitative trends. At low momentum-flux ratio (*IR* = 0.65) the coolant emerges from the hole with limited dispersal to the mainstream. In practice this would provide a metal temperature similar to that of the coolant and minimise the heat transfer to the wall. At *IR* = 2.6 the coolant plume has increased momentum and the boundary layer has visibly thinned on both sides of the jet; there will be a corresponding increase in heat transfer coefficient. Mainstream flow is entrained into the centre of the jet and this intensifies with increasing *IR*. The kidney vortices are apparent for *IR* = 2.6 in the data for both rigs at similar locations: $y/D \approx 0.5$ and $z/D \approx 0.4$. These vortices are more intense at *IR* = 4.5; data from the two rigs show differences in the degree of penetration of the jet into the main-flow and in the magnitude of the red high-velocity region seen for *IR* = 4.5. This is possibly a consequence of the lower spatial resolution of the volumetric velocimetry technique. The velocity vectors in this region are a result of an average of vectors contained in a larger volume than S-PIV. This difference is made more distinct by the local validation processing and overlap plotting employed to achieve the results of Bernsdorf *et al.* [13]. As stated previously, no filters were employed in the volumetric velocimetry results presented in this paper.

Differences are also observed in the regions near the wall, mainly due to the dissimilar boundary layers. Whilst the boundary in the current results has a shape factor of H = 1.29 closely following the 1/7th power law (see Figure 6), Bernsdorf *et al.* [13] have a shape factor of H = 2.3, which implies a less full boundary layer profile, with lower velocities for the same y/δ and typical of a more adverse pressure gradient. The comparison between the two experimental campaigns is highlighted in Table 2.

4.2 Effect of Momentum-Flux Ratio, *IR*

Figure 8 shows data plotted in a similar form to that in Figure 7 but at a plane located x/D = 6 downstream of the

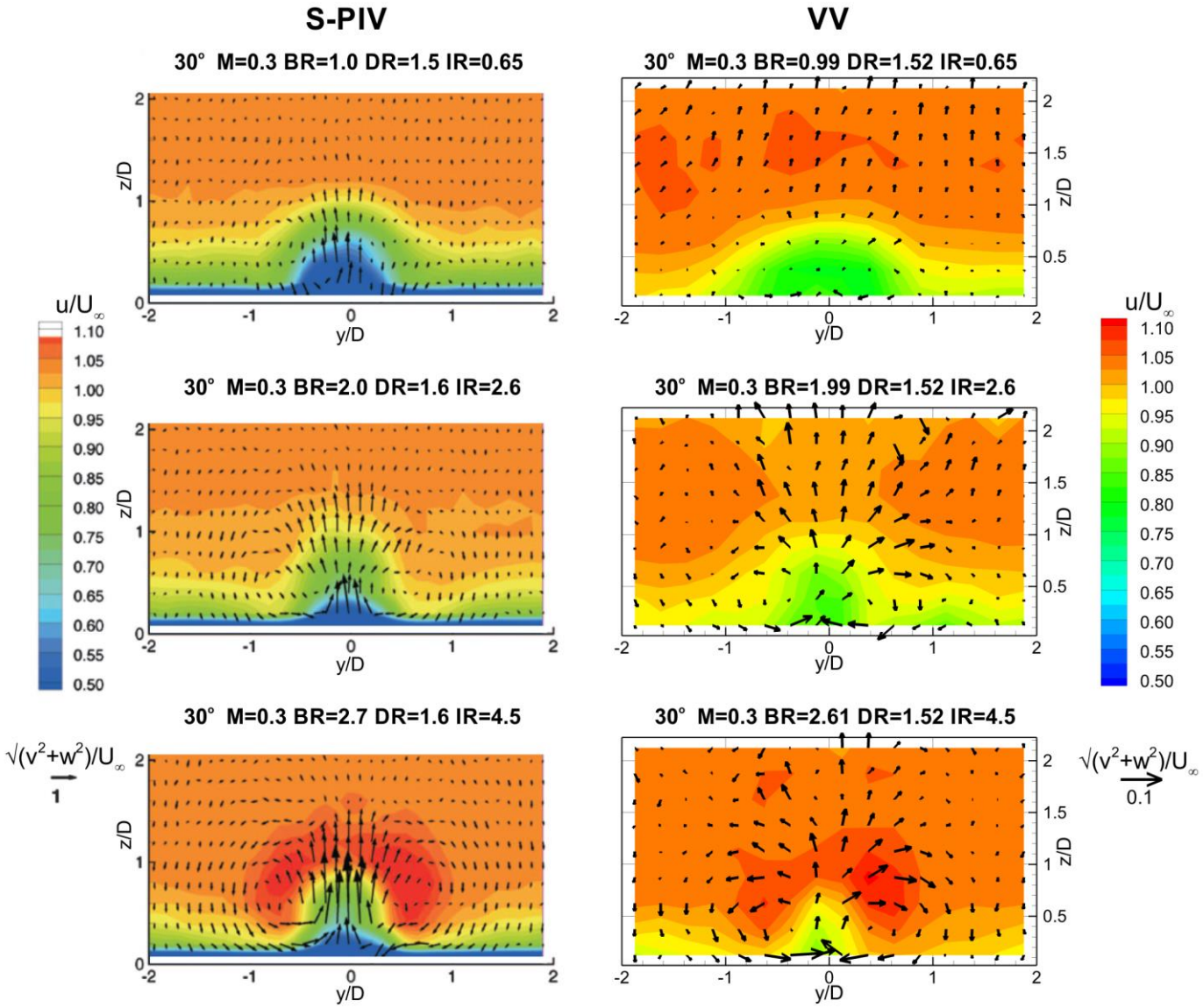

Figure 7: Comparison of S-PIV [13] and VV at *x/D* = 4

hole. Data for 0.65 < *IR* < 6.5 is shown. The contour levels used in Figure 8 are different to those in Figure 7, which were specifically chosen for close comparison with Bernsdorf *et al.* [13].

The flow structure for the different cases is consistent with the descriptions in the literature. For very low *IR* the jet remains attached to the wall, thickening the boundary layer. The main flow is displaced upwards as a result. Entrainment of the main flow is insignificant, resulting in efficient film cooling at the surface. For *IR* = 0.65, a small component of velocity is visible in the bottom line of vectors and near the centre, pointing towards the centreline. This suggests a very weak vortex near the wall. The secondary-flow features are intensified with increasing *IR* and for the subsequent cases the vectors in this region are increasingly stronger until a clear vortex is seen for *IR* = 2.6. A region of lower velocity (in blue), seen for *IR* = 0.65 dominating the centre of the jet near the wall shrinks as *IR* is increased and eventually disappears for *IR* = 3.5 as the velocities in the entire volume steadily increase for higher *IR*. As *IR* increases, the jet breaks away from the boundary layer, forming strong kidney vortices. This shows the entrainment of the main flow becoming increasingly more pronounced.

The centre of the kidney vortices remains relatively constant at $y/D \approx 0.5$, with a marginal drift away from the centreline with increasing *IR*. In contrast, there is a pronounced shift in the *z* direction: the centre of the vortex is displaced from $z/D \approx 0.6 \rightarrow 0.85$ as *IR* increases from $3.5 \rightarrow 6.5$. The thickness of the boundary layer decreases with increasing *IR*, as the kidney vortices progressively dominate the flow.

For *IR* = 4.5 and above, a region of higher velocity caps the top surface of the jet. In all cases the vector magnitude of the in-plane vectors is significantly lower than the *u* component.

The contour for $u/U_\infty \approx 1$ (shown in yellow) illustrates how the flow structure changes with *IR*. For *IR* = 0.65 this curve is smoothly displaced upwards. This displacement becomes more pronounced, with sharper curvature, for $IR = 1.6 \rightarrow 2.6$. For *IR* > 3.5 there is an inflection in the curve as the boundary layer progressively thins with greater entrainment and the kidney vortices gain strength. The core

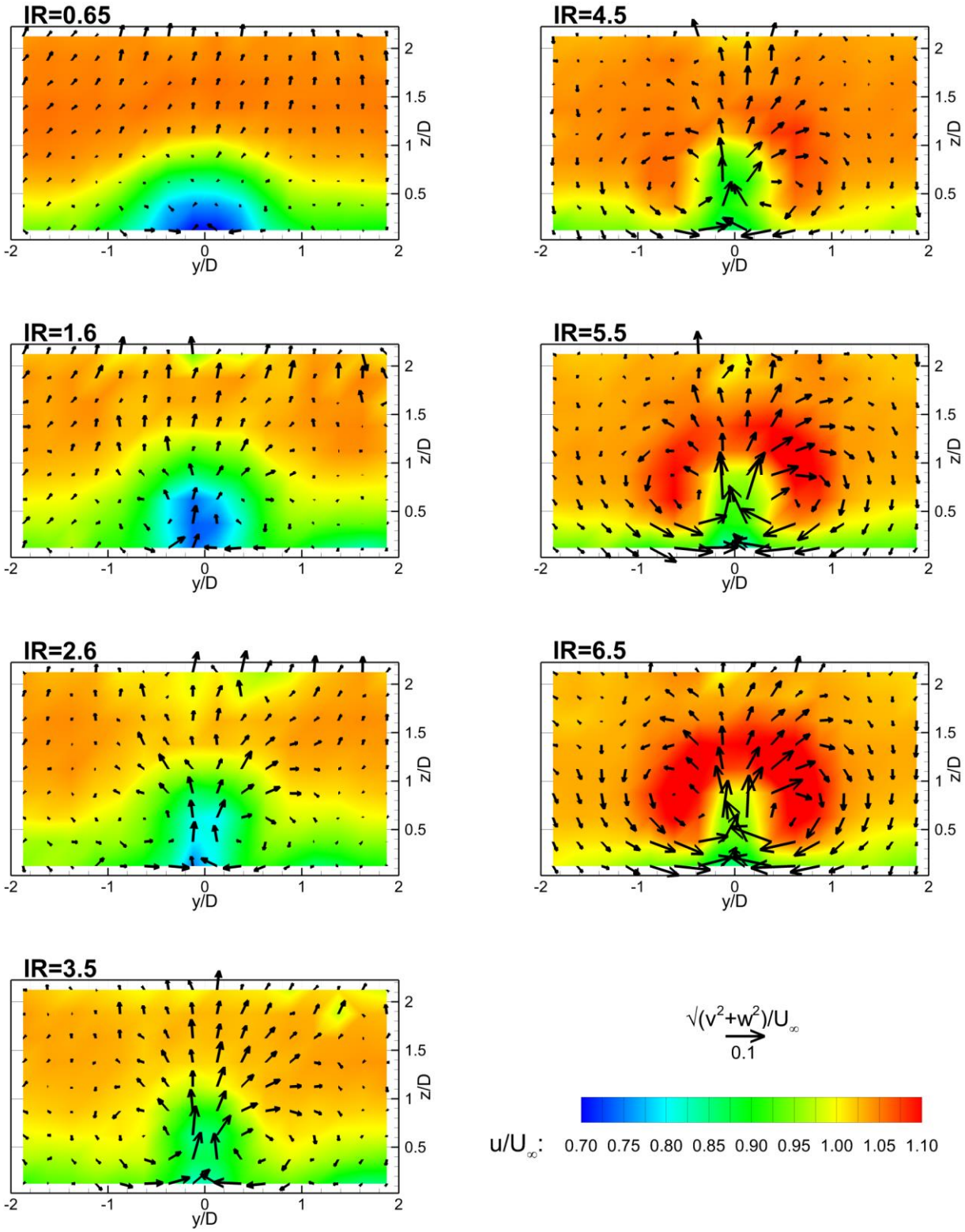

Figure 8: *x/D* = 6 for all cases

of the jet shrinks in width but maintains a similar height as *IR* increases.

Figure 9 shows stacked streamwise planes at positions *x/D* = 2, 4, 6 and 8 on top with a cross-stream plane for *y/D* = 0 below for the cases *IR* = 0.65, 1.6, 3.5 and 6.5. The streamwise planes provide an overview of the development of jet and associated fluid-dynamic structures downstream of the hole. The cross-stream planes show the evolution of the jet and in particular the centre line of the jet with a contour of u/U_∞ that highlights the difference in flow velocity between a case with low *IR* to a case with higher *IR*.

For *IR* = 0.65 the region of lower velocity near the wall, in blue, expands in height for planes farther away from the film cooling hole. In fact, the core of the jet can be seen expanding for the other cases as well. On the other hand, the thickness of the boundary layer remains constant through *x*.

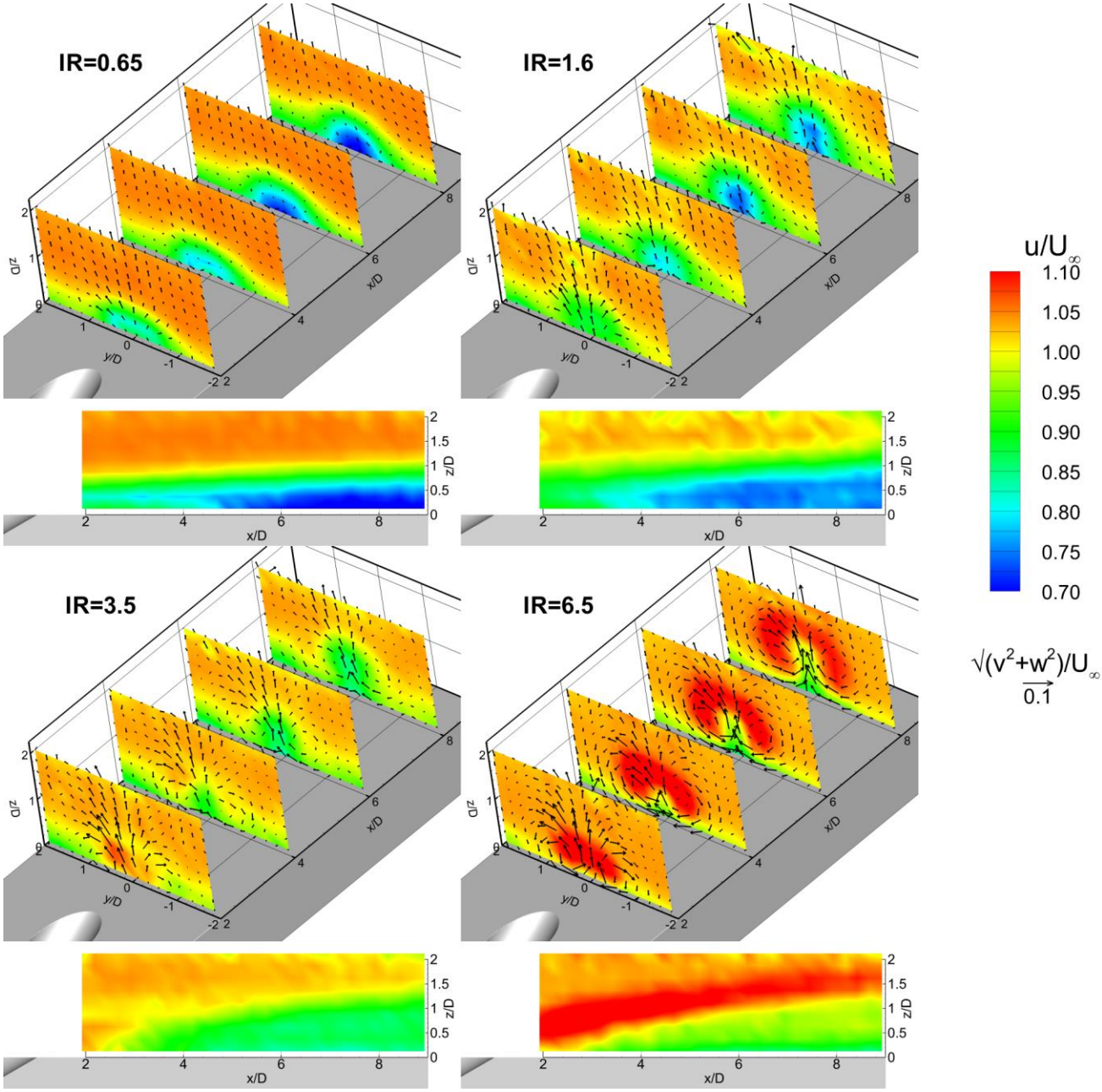

Figure 9: *x/D* = 2, 4, 6 & 8 (top) and *y/D* = 0 (bottom) for *IR* = 0.65, 1.6, 3.5 & 6.5

At *x/D* = 2 the velocity vectors of the expanding jet are visible around the centre line, near the wall. This effect has faded at *x/D* = 4.

For *IR* = 1.6 the behaviour of the jet has changed substantially with strong *w*-component vectors around the centreline, suggesting the flow is now detached. Similar behaviour is observed for *IR* = 3.5 and 6.5, where the jet has broken through the boundary layer. The flow at *x/D* = 2 is dominated by vectors of higher magnitude pointing outward. However, in these cases, the remaining slices show kidney vortices, with higher velocity vectors in *v* and *w* for higher momentum flux ratio. The *u* component also changes accordingly, with the region of higher velocity seen around the jet increasing with *IR* = 6.5.

The plots for *y/D* = 0 provide more insight into the different flow behaviour observed for different *IR*. For the first case the coolant flow seems to merge smoothly with main flow boundary layer. However, for *IR* = 1.6 there is a very clear shift of the main flow around a solid obstacle: the difference in this case is that the coolant interacts with the deflected air and fluid is entrained. For *IR* = 3.5 and 6.5 the jet deflection is very evident. After full detachment of the jets the flow behaviour remains similar for increasing *IR*, differing only in the magnitude of the velocity vectors. The jet penetration increases considerably from *IR* = 0.65 to *IR* = 1.6, with only a small difference among the remaining cases. This eventually leads to a region of higher velocity flow seen curving on the top of the jet, as shown for *IR* = 6.5.

For *IR* = 0.65 near the wall between *x/D* = 2 and *x/D* = 5 a region of higher velocity flow is visible. The velocity is elevated slightly by $u/U_\infty \approx 0.1$. Similar behaviour is also observed for *IR* = 1.6, but between *x/D* = 2 and *x/D* = 3.

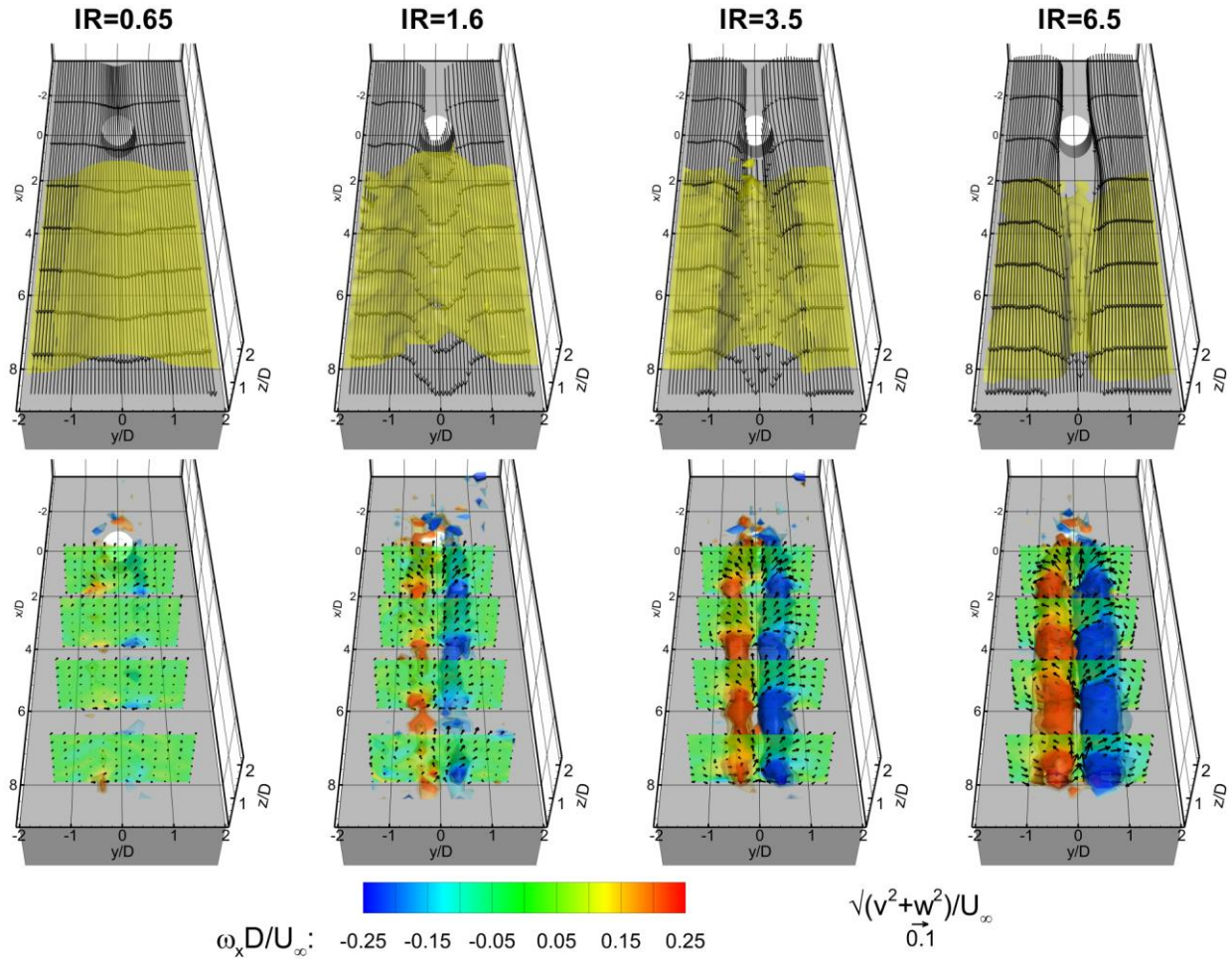

Figure 10: Isosurfaces of *u/U* = 1.00 (top) and ω_x = ±0.15, ±0.20, ±0.25 (bottom) for *IR* = 0.65, 1.6, 3.5 & 6.5

During the experiments a separation bubble was observed aft of the exit of the hole that trapped the seeding flow, causing unwanted reflections requiring this region to be removed from the images and therefore measurements. The size of this separation bubble decreased with increasing IR and is representative of real flow behaviour. It may be hypothesized that the higher velocity region observed is due to this separation bubble. This will be the subject of further investigation.

The top row of Figure 10 shows the isosurface for u/U_∞ = 1.0 for *IR* = 0.65, 1.6, 3.5 and 6.5. Streamlines are also shown in these plots. These were defined as a rake passing in a line at constant *z/D* = 0.5 and *x/D* = 8, with 50 streamlines plotted between *y/D* = -1.75 and *y/D* = +1.75. The bottom row of Figure 10 shows the stream-wise vorticity (ω_x) with isosurfaces at constant non-dimensional value of ±0.15, 0.20 and 0.25. These clearly track the counter-rotating cores of the kidney vortices. Superposed are in-plane vectors and contours of vorticity for planes at *x/D* = 2, 4, 6 and 8. The vorticity colour bar shown in figure 10 applies both to the planes and the isosurfaces in the bottom row.

The isosurface of velocity for *IR* = 0.65 shows a gentle deflection where the coolant is ejected into the mainstream. The streamlines and vorticity reveal very weak secondary-flow features, in particular, a very weak nascent kidney vortex like structure very close to the surface. The streamlines demonstrate minimal blockage at this height. For *IR* = 1.6 the behaviour changes significantly. The velocity isosurface shows a much stronger deflection around the centreline; this deflection shows strong symmetric inflection points for *IR* = 3.5 → 6.5. The growth in the strength and size of the kidney vortices is clearly shown for higher *IR*. The centre of the kidney vortices is seen to shift as *IR* increases from 1.6 → 6.5. The streamlines show the entrainment of main-flow into the jet, especially for *IR* = 3.5 → 6.5. The blockage created by the jet is also observed by the lack of streamlines upstream of the hole.

4.3 Kidney Vortices

One of the principal advantages of VV is its ability to accurately capture three dimensional flow features, in this case the kidney vortices. To understand the behaviour of these kidney vortices the location of the vortex centre and the vortex circulation will be extracted as a function of momentum flux ratio. This will elucidate the vortex growth, lift-off and decay.

In order to track the core of the counter-rotating vortices, the method develop by Graftieaux *et al.* [30] and described in Morgan *et al.* [31] was applied across the y-z planes between *x/D*=0 and *x/D*=8. Graftieaux *et al.* [30] define the dimensionless scalar function Γ_2:

$$\Gamma_2(P) = \frac{1}{N}\sum_S \frac{\left[\overrightarrow{PM} \times \left(\overrightarrow{V_M} - \overrightarrow{V_P}\right)\right].\vec{n}}{\left\|\overrightarrow{PM}\right\|.\left\|\overrightarrow{V_M} - \overrightarrow{V_P}\right\|}$$

Where $\vec{n}$ is the normal to the plane and *M* represents each of the *N* points included in the area of integration *S* around the point *P*. $\overrightarrow{V_M}$ is the velocity vector at each point *M*, whilst $\overrightarrow{\tilde{V}_P}$ is a local convection velocity around *P*, given by:

$$\overrightarrow{\tilde{V}_P} = \frac{1}{N}\sum_{S} \overrightarrow{V_M}$$

An area of integration containing *N* points, with a maximum $\Gamma_2(P)$, with a size similar to the vortex is then applied and the following weighted average used to find the vortex core:

$$y_{centre} = \frac{\sum_{i=1}^{N} y_i \Gamma_{2_i}}{\sum_{i=1}^{N} \Gamma_{2_i}}$$

$$z_{centre} = \frac{\sum_{i=1}^{N} z_i \Gamma_{2_i}}{\sum_{i=1}^{N} \Gamma_{2_i}}$$

In order for this vortex region to be correctly identified, the mean $\mu(\Gamma_2)$ and standard deviation $\sigma(\Gamma_2)$ are taken for each plane. For a vortex with positive circulation, only points with a circulation $\Gamma_2 > \mu(\Gamma_2) + \sigma(\Gamma_2)$ are considered; for a vortex with negative circulation the condition $\Gamma_2 > \mu(\Gamma_2) - \sigma(\Gamma_2)$ is applied.

The circulation Γ ($\Gamma = \oiint \omega_x \, dS$) is calculated in the area S that encompasses the vortex using the trapezium rule.

The measurements of y_{centre}, z_{centre} and Γ are shown in figure 11. The momentum flux ratios are the same as for figures 6 and 7. For each case, the vortex with positive circulation is plotted with solid line and solid markers, whilst the vortex with a negative circulation is plotted with dashed line and open markers.

The y_{centre}/D coordinates of the vortex are shown in Figure 11a. For *IR* = 0.65 the two vortices emanate from the edges of the hole and are therefore initially separated by y/D ~ 1, but as they progress downstream they converge on the symmetry plane, reaching *y/D* ~ 0 at *x/D* ~ 5.5. There is a lot of uncertainty in the vortex identification for this low momentum flux ratio because the vortices are so weak and indistinct, as shown in Figure 10. With increasing momentum flux ratio the vortices all start from a similar location but rather than converging on the symmetry plane they begin to diverge. This effect is most prominent for *IR* = 6.5 where the vortices start with a separation of *y/D* ~ 1 but by *x/D* = 8 this has increased to *y/D* ~ 1.4.

The z_{centre}/D coordinates of the vortex are shown in Figure 11b. For *IR* = 0.65 the vortex identification algorithm is initially subject to noise due to the weak, incoherent vortex but then converges on a relatively constant value of z/D ~ 0.25. It is therefore always close to the wall. With the momentum flux ratio increased to *IR* = 1.6 the vortex begins to lift off the wall. Further increase in momentum flux ratio results in a monotonic lift off of the kidney vortex pair from the wall.

The absolute circulation normalised by the hole diameter and freestream velocity is shown in Figure 11c. The positive and negative vortices show slightly different values of circulation for each case, which could indicate a slight asymmetry in the experimental setup. Every effort was made to ensure symmetry with all components being symmetrical except for the outlet duct. This outlet duct was studied through RANS CFD and demonstrated to have no effect on symmetry within the test section. This has been corroborated

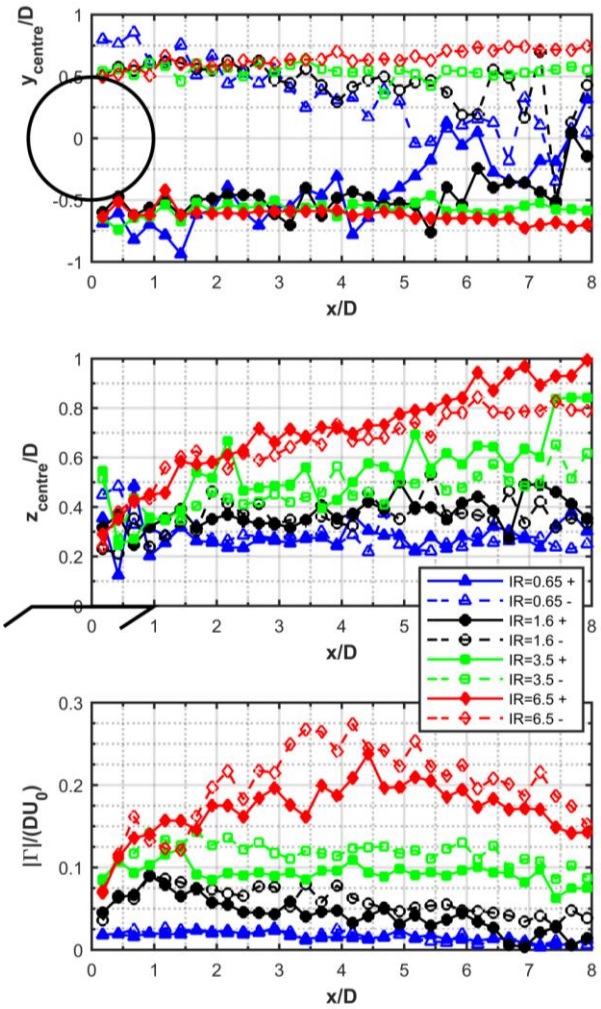

Figure 11: Vortex core location *(x/D, y/D, z/D)* and Circulation *Γ* for *IR* = 0.65, 1.6, 3.5 & 6.5

through VV, pressure and hot wire measurements in the test section that have all demonstrated symmetry in the freestream. An alternative is asymmetry in the cooling holes. These were manufactured to a H12 tolerance with the three holes fed from a single settling chamber. Again every effort was made to ensure symmetry including a symmetrical design, CFD studies and turbulence screen but it is possible there is a small difference in mass flow between the three holes. Nevertheless, the effect of the asymmetry is small and does not affect the conclusions which are drawn from the measurements.

For *IR* = 0.65, the value of circulation is generally very low. Nevertheless, this circulation clearly decays reaching a value close to zero around *x/D* ~ 7. It is not possible to discern a peak outside the bounds of experimental uncertainty. With increasing momentum flux ratio there are clear monotonic trends of increasing peak circulation at a later x/D followed by decay. For *IR* = 1.6 there is a clear peak at *x/D* = 1, followed by a continuous decay in circulation. This peak grows in magnitude and shifts to *x/D* = 1.5 and *x/D* = 4 for *IR* = 3.5 and 6.5 respectively. This behaviour is indicative of an initial roll up phase followed by decay and vortex breakdown [32, 33]. With higher momentum flux ratios, the roll up phase takes longer and the peak circulation is higher. The combination of a vortex with a counter-rotating vortex in a

pair / dipole will produce a self-induced vertical velocity according to:

$$V_{ind} = \frac{\Gamma}{4\pi d_s}$$

Where d_s is the distance to the symmetry plane. In the case of $IR = 6.5$ applying this equation with the measurements of separation and circulation gives a cumulative vertical z-displacement of $0.18D$ over the range $x = 0D$ to $8D$. It is therefore a minor contributing factor to the propagation of the kidney vortices into the freestream. The dominant factor is instead the vertical momentum from the film cooling jet.

Similarly, the wall will act as a mirror plane in effect producing two vortex dipoles with self-induced horizontal velocities outwards from the hole. The effect of this wall-vortex interaction can be quantified by applying the dipole velocity equation to the experimental measurements. This yield contributions at x/D = 8 to the lateral vortex separation (y-distance between vortex centres) of: 0.08D, 0.17D, 0.27D and 0.36D for IR = 0.65, 1.6, 3.5 and 6.5 respectively. In fact, the low momentum flux ratios experience a decrease in lateral separation indicating that this is a weak effect and instead these flows are dominated by the exchange of linear momentum which acts to converge the vortices. However, the IR = 6.5 case experiences a divergence indicating that the vortex is now much more dominant, see Figure 9. Indeed the experimental measurement yields a lateral separation of 0.31D relative to the self-induced velocity contribution of 0.36D indicating that the vertical flow is now dominant so that its self-induced velocity is the major contributing factor to the lateral separation. At low momentum flux ratios the momentum from the film cooling jet is insufficient to produce a strong free vortex pair and this behaviour is instead overwhelmed by the momentum in the freestream. For example, $IR = 1.6$ initially obeys the self-induced velocity trend but after $x/D = 3$ becomes overwhelmed by the freestream and begins to converge, and $IR = 0.65$ produces a weak indistinct vortex pair that is trapped on the wall. These cases cannot therefore be described as having free vortex.

5 THE USE OF VOLUMETRIC VELOCIMETRY IN TURBOMACHINERY APPLICATIONS

Section 4 has demonstrated the capability of VV for capturing highly three-dimensional flows and the insight this can give. In order to quantify the merits of VV, Table 4 provides reasonable estimates of the performance relative to comparable laser techniques for application to the same film cooling facility using equipment available at the University of Bath.

The maximum vector resolution for PIV and S-PIV are based on an interrogation spot size of 32 x 32 pixels. The velocity uncertainty is for a single volume capture. For VV this is estimated as described in Section 2.1; for LDV, PIV and S-PIV it is estimated by propagating measurement uncertainties using references [34-36]. It should be noted that for S-PIV, the uncertainty in Δz makes a significantly greater contribution than the error propagation terms involving Δx and Δy (unlike VV). We estimate the uncertainty in Δz for S-PIV to be ≈ 25 times more significant than in VV.

The experimental time is estimated for a single capture of a volume of equal size and resolution to the test case in the present study with the assumption of automated traverses for LDV, PIV and S-PIV.

Depending on the experiment criteria, each technique has its own niche advantage. LDV for capturing high-frequency phenomenon, PIV for quickly capturing predominantly two-dimensional phenomenon and S-PIV for capturing planar measurements of 3D phenomena. However, for highly three-dimensional, time-averaged, phenomena VV has the advantage of lower acquisition times and equal, low, uncertainty in all directions. This makes it very well suited to turbomachinery applications where acquisition time is precious and highly three-dimensional flows expected. Furthermore, for instantaneous / unsteady measurements VV has the advantage of simultaneously capturing an entire volume whereas LDV, PIV and S-PIV rely on interpolating time-averaged data onto a structured grid which loses transient flow features. VV is therefore particularly appropriate to turbomachinery applications where highly 3D flow features are dominant and unsteady features may be of interest.

6 CONCLUSIONS

Volumetric velocimetry was successfully employed to study steady-state film cooling including the effect of momentum flux ratio. A new facility was designed and commissioned in order to apply this novel measurement technique. It was possible to resolve the highly complex 3D flow features typical of film cooling, including those dependent on the much smaller *v* and *w* components. The results show the same trends recorded in the literature regarding the behaviour of the jet for different momentum flux ratios. In particular the increasing jet penetration, blockage effects and increasing strength of the kidney vortices with increasing momentum flux ratio are all clearly demonstrated.

Table 4: Estimates of experimental performance for laser measurement techniques applied to the film cooling facility. Values are estimates for state of the art TSI equipment available through the University of Bath VFMS instrument pool.

Characteristic	LDV	PIV	S-PIV	VV
Spatial dimensionality	0D	2D	2D	3D
Number of vector components	≤ 3	2	3	3
Time-averaged vector resolution	~ 1 mm [34]	~ 0.6 mm	~ 0.6 mm	1 mm
Sample Rate	> 2 kHz [34]	8 Hz	8 Hz	8 Hz
Uncertainty in instantaneous $\lvert\vec{V}\rvert$	~ ± 1 % [35]	~ ± 1 % [34]	~ ± 6 % [36]	± 3 %
Setup & calibration time	30 minutes	2 hours	5 hours	5 hours
Data acquisition time	18 hours	33 hours	8 hours	1 minute
Processing time	< 30 minutes	1 hour	2 hours	12 hours
Capable of volume resolved transient features	No	No	No	Yes

At low momentum flux ratios the kidney vortices are weak, indistinct, remain close to the wall, and quickly decay to zero whilst converging on the symmetry plane. With increasing momentum flux ratio the circulation increases with the roll up phase taking longer, and the vortices lift off from the wall and begin to diverge laterally. The self-induced velocity of the kidney vortex pair makes a minor contribution to the vertical lift-off; but the self-induced velocity created by the wall-vortex interaction is a major contributing factor to the lateral divergence.

Volumetric velocimetry is demonstrated to be a very powerful technique well suited to capturing highly three-dimensional turbomachinery flows. It is particularly applicable to scenarios where unsteadiness is of interest.

ACKNOWLEDGMENTS

The authors would like to thank Andrew Langley, Stephen Thomas, Vijay Rajput and all other technicians involved in the manufacture and assembly of the film cooling rig. The VV measurements presented in this paper could not have been achieved without the support of Dr. Martin Hyde and TSI. The research described here was supported by the *Engineering and Physical Sciences Research Council* (EPSRC) through grant number EP/M026345/1. The VV system is part of the *Versatile Fluid Measurement System* (VFMS), acquired through the EPSRC Strategic Equipment Panel (grant number EP/K040391/1). Data access: Due to confidentiality agreements with research collaborators, supporting data can only be made available to bona fide researchers subject to a nondisclosure agreement. Details of how to request access are available at the University of Bath data archive website[1].

NOMENCLATURE

a	speed of sound
BR	blowing ratio $\left(BR = \frac{\rho_c U_c}{\rho_m U_m}\right)$
d	distance to the reference frame origin
D	hole diameter
DR	density ratio $\left(DR = \frac{\rho_c}{\rho_m}\right)$
g	hole pitch
H	shape factor
IR	momentum flux ratio $\left(IR = \frac{\rho_c U_c^2}{\rho_m U_m^2}\right)$
l	hole length
M	Mach number $\left(M = \frac{U_\infty}{a}\right)$
$\vec{r}$	displacement vector
Ra	surface roughness
St	Stokes number $\left(St = \frac{\tau}{\tau_{fts}}\right)$
u	streamwise component of velocity
U	velocity magnitude
U_∞	freestream velocity
v	lateral component of velocity
$\vec{V}$	velocity vector
$\sqrt{v^2 + w^2}$	velocity magnitude in a YZ plane
w	vertical component of velocity
x	streamwise coordinate
Δx	displacement in x
y	lateral coordinate
y_{centre}	y-coordinate of vortex centre
Δy	displacement in y
z	vertical coordinate
z_{centre}	z-coordinate of vortex centre
Δz	displacement in z
α	hole angle
Γ	circulation ($\Gamma = \oiint \omega_x \, dS$)
Γ_2	dimensionless scalar function [30]
δ	boundary layer thickness
δ^*	displacement thickness
Δt	laser pulse time-step
ζ	azimuthal angle ($\zeta = \tan^{-1}(y/x)$)
θ	momentum thickness
σ	standard deviation
ς	uncertainty
τ	characteristic response time of a particle
τ_{fts}	characteristic flow time-scale
φ	polar angle ($\varphi = \cos^{-1}(z/\lvert\vec{r}\rvert)$)
ω_x	streamwise component of vorticity $\left(\omega_x = \frac{dw}{dy} - \frac{dv}{dz}\right)$

Subscripts

c	coolant flow
m	main flow

REFERENCES

[1] T. Fric and A. Roshko, "Vortical structure in the wake of a transverse jet," *Journal of Fluid Mechanics*, vol. 279, pp. 1-47, 1994.

[2] J. Andreopoulos and W. Rodi, "Experimental investigation of jets in a crossflow," *Journal of Fluid Mechanics*, vol. 138, pp. 93-127, 1984.

[3] D. Bogard and K. Thole, "Gas turbine film cooling," *Journal of propulsion and power*, vol. 22, no. 2, pp. 249-270, 2006.

[4] R. S. Bunker, "A review of shaped hole turbine film-cooling technology," *Transactions of the ASME-C-Journal of Heat Transfer*, vol. 127, no. 4, p. 441, 2005.

[5] G. Wilfert and L. Fottner, "The aerodynamic mixing effect of discrete cooling jets with mainstream flow on a highly loaded turbine blade," in *ASME 1994 International Gas Turbine and Aeroengine Congress and Exposition*, 1994, pp. V001T01A084-V001T01A084: American Society of Mechanical Engineers, 1994

[6] F. L. Peña and T. Arts, "On the Development of a Film Cooling Layer," *Heat Transfer and Cooling in Gas Turbines, AGARD CP-527, ref. 36*, 1993.

[7] R. J. Goldstein, E. R. G. Eckert, and F. Burggraf, "Effects of hole geometry and density on three-dimensional film cooling," *International Journal of Heat and Mass Transfer*, vol. 17, no. 5, pp. 595-607, 1974.

[8] A. Kohli and D. G. Bogard, "Adiabatic Effectiveness, Thermal Fields, and Velocity Fields for Film Cooling With Large Angle Injection,"

[1] http://dx.doi.org/10.15125/BATH-00116

Journal of Turbomachinery, vol. 119, no. 2, pp. 352-358, 1997.

[9] D. K. Walters and J. H. Leylek, "A Detailed Analysis of Film-Cooling Physics: Part I-Streamwise Injection With Cylindrical Holes," in *ASME 1997 International Gas Turbine and Aeroengine Congress and Exhibition*, 1997, pp. V003T09A052-V003T09A052: American Society of Mechanical Engineers, 1997.

[10] K. T. McGovern and J. H. Leylek, "A detailed analysis of film cooling physics: Part II-Compound-angle injection with cylindrical holes," *Journal of Turbomachinery*, vol. 122, no. 1, pp. 113-121, 2000.

[11] D. G. Hyams and J. H. Leylek, "A detailed analysis of film cooling physics: Part III-streamwise injection with shaped holes," in *ASME 1997 International Gas Turbine and Aeroengine Congress and Exhibition*, 1997, pp. V003T09A054-V003T09A054: American Society of Mechanical Engineers, 1997.

[12] J. Woisetschläger and E. Göttlich, "Recent Applications of Particle Image Velocimetry to Flow Research in Thermal Turbomachinery," in *Particle Image Velocimetry*: Springer, 2007, pp. 311-331.

[13] S. Bernsdorf, M. G. Rose, and R. S. Abhari, "Modeling of Film Cooling-Part I: Experimental Study of Flow Structure," *Journal of Turbomachinery*, vol. 128, no. 1, pp. 141-149, 2005.

[14] M. K. Eberly and K. A. Thole, "Time-resolved film-cooling flows at high and low density ratios," *Journal of Turbomachinery*, vol. 136, no. 6, 2013.

[15] B. Laveau and R. S. Abhari, "Influence of flow structure on shaped hole film cooling performance," vol. 4, ed, 2010, pp. 1677-1689.

[16] L. M. Wright, S. T. McClain, C. P. Brown, and W. V. Harmon, "Assessment of a double hole film cooling geometry using S-PIV and PSP," vol. 3, ed, 2013.

[17] R. P. Schroeder and K. A. Thole, "Effect of High Freestream Turbulence on Flowfields of Shaped Film Cooling Holes," *Journal of Turbomachinery*, vol. 138, no. 9, p. 091001, 2016.

[18] D. Cleaver, Z. Wang, and I. Gursul, "Oscillating flexible wings at low Reynolds numbers," in *51st AIAA Aerospace Sciences Meeting*, 2013: University of Bath.

[19] D. E. Calderon, Z. Wang, I. Gursul, and M. R. Visbal, "Volumetric measurements and simulations of the vortex structures generated by low aspect ratio plunging wings," 2013.

[20] T. Boushaki, A. Koched, Z. Mansouri, and F. Lespinasse, "Volumetric velocity measurements (V3V) on turbulent swirling flows," *Flow Measurement and Instrumentation*, vol. 54, pp. 46-55, 2017.

[21] M. Stellmacher and K. Obermayer, "A new particle tracking algorithm based on deterministic annealing and alternative distance measures," *Experiments in Fluids*, vol. 28, no. 6, pp. 506-518, 2000.

[22] S. Bernsdorf, "Experimental Investigation of Film Cooling Flow Structure," Doktor der Wissenschaften, Eidgenossischen Technischen Hochschule Zurich, 2005.

[23] C. Tropea, A. L. Yarin, and J. F. Foss, *Springer handbook of experimental fluid mechanics*. Springer Science & Business Media, 2007.

[24] R. Moffat, "Contributions to the theory of single-sample uncertainty analysis," *ASME, Transactions, Journal of Fluids Engineering*, vol. 104, no. 2, pp. 250-258, 1982.

[25] R. Moffat, "Using uncertainty analysis in the planning of an experiment," *ASME, Transactions, Journal of Fluids Engineering(ISSN 0098-2202)*, vol. 107, pp. 173-178, 1985.

[26] R. Moffat, "Describing the uncertainties in experimental results," *Experimental thermal and fluid science*, vol. 1, no. 1, pp. 3-17, 1988.

[27] H. Ito, Y. Watanabe, and Y. Shoji, "A long-radius inlet nozzle for flow measurement," *Journal of Physics E: Scientific Instruments*, vol. 18, no. 1, p. 88, 1985.

[28] R. D. Mehta and J. H. Bell, "Boundary-layer predictions for small low-speed contractions," *AIAA journal*, vol. 27, no. 3, pp. 372-374, 1989.

[29] R. D. Mehta and P. Bradshaw, "Design rules for small low speed wind tunnels," *The Aeronautical Journal (1968)*, vol. 83, no. 827, pp. 443-453, 1979.

[30] L. Graftieaux, M. Michard, and N. Grosjean, "Combining PIV, POD and vortex identification algorithms for the study of unsteady turbulent swirling flows," *Measurement Science and technology*, vol. 12, no. 9, p. 1422, 2001.

[31] C. Morgan, H. Babinsky, and J. Harvey, "Vortex detection methods for use with PIV and CFD data," in *47th AIAA Aerospace Sciences Meeting, Orlando, Florida*, 2009.

[32] A. Karagozian, "An analytical model for the vorticity associated with a transverse jet," *AIAA journal*, vol. 24, no. 3, pp. 429-436, 1986.

[33] B. Zang and T. H. New, "Near-field dynamics of parallel twin jets in cross-flow," *Physics of Fluids*, vol. 29, no. 3, p. 035103, 2017.

[34] N. Pedersen, P. S. Larsen, and C. B. Jacobsen, "Flow in a centrifugal pump impeller at design and off-design conditions—part I: particle image velocimetry (PIV) and laser Doppler velocimetry (LDV) measurements," *Journal of Fluids Engineering*, vol. 125, no. 1, pp. 61-72, 2003.

[35] K. Thole, M. Gritsch, A. Schulz, and S. Wittig, "Flowfield measurements for film-cooling holes with expanded exits," *Journal of turbomachinery*, vol. 120, no. 2, pp. 327-336, 1998.

[36] A. Prasad and R. Adrian, "Stereoscopic particle image velocimetry applied to liquid flows," *Experiments in fluids*, vol. 15, no. 1, pp. 49-60, 1993.